Real Time Estimator of Winding Hotspot Temperature for PMSM Drives

Real Time Estimator of Winding Hotspot Temperature for PMSM Drives

Paolo Pescetto
Dipartimento Energia Galileo Ferraris
Politecnico di Torino
Turin, Italy
paolo.pescetto@polito.it

Gaetano Dilevrano
Dipartimento Energia Galileo Ferraris
Politecnico di Torino
Turin, Italy
gaetano.dilevrano@polito.it

Gianmario Pellegrino
Dipartimento Energia Galileo Ferraris
Politecnico di Torino
Turin, Italy
gianmario.pellegrino@polito.it

Aldo Boglietti
Dipartimento Energia Galileo Ferraris
Politecnico di Torino
Turin, Italy
aldo.boglietti@polito.it

***Abstract*—The electrical drives for high-performance applications often present a relevant temperature gradient within the stator winding. If a thermistor is often embedded in the machine, the hottest winding point is normally not accessible, leading to the need for high thermal safety margins, and so arming the full exploitation of the machine's torque capability. To solve this issue, the present work deals with hotspot temperature monitoring and prediction for synchronous motor drives. An advanced Lumped Parameter Thermal network is proposed, modeling the thermal gradient inside the stator. An automatic calibration procedure is presented, based on simple thermal commissioning tests. Experimental results on a high-performance traction PMSM demonstrate the effective capability of dynamically tracking the hotspot temperature, with a residual error <5°C, thus enabling the full and safe exploitation of the motor overload capabilities.**

***Index Terms*—Thermal model, Short time thermal transient, hotspot temperature estimation, temperature observer**

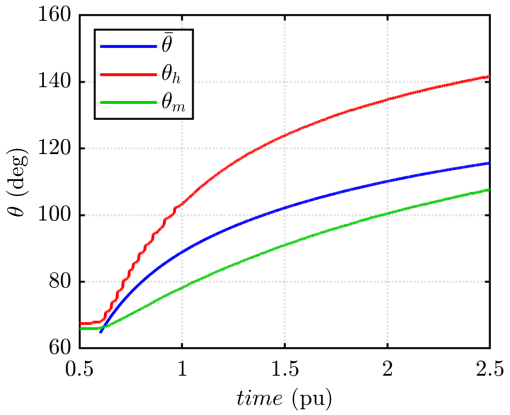

Fig. 1. Example of thermal transient on the MUT.

I. Introduction

In modern high-performance motor drives, the increasing power density requires advanced thermal modeling and management of the machine [1]–[4]. From a thermal perspective, the stator winding is commonly among the most critical components, and its temperature must be limited for avoiding faults or premature aging of the insulation [5]–[7]. Moreover, highly compact drives may present a relevant thermal gradient inside the stator winding, that should be considered [8]. To prevent thermal failure, the stator winding temperature can be monitored either through direct measurements or by real-time temperature observers, to be executed within the motor control routine [9].

To avoid overheating the drive, even during transient overload, several real-time observers are found in the literature for estimating the inverter [10], PM [11] and winding temperature [12], [13], e.g. based on the estimation of the stator resistance variation or on the dynamic inductance. This permits actively limiting the temperature of the sensitive components by limiting the inverter current, and eventually monitoring the state of health of the drive [14]. Anyway, techniques like [12], [13] are only capable of estimating the average winding temperature, thus neglecting its thermal gradient. Most traction motors embed one or more winding thermistors, but the hottest point is often not accessible in highly compact machines [15]. Therefore, the measured temperature does not refer to the most critical point. In particular, the Motor Under Test (MUT) embeds a single thermistor in the only accessible winding point, but the motor presents a hotspot reaching a considerably higher temperature, even larger than 50°C. In addition, the overtemperature of the hotspot dynamically varies during operation, depending on the motor operating conditions. An example is shown in Figure 1, reporting the thermal response to a step load torque, corresponding to a step increase in the losses. The picture reports the average winding temperature $\bar{\theta}$, and the temperatures of the hotspot θ_h and measurable θ_m points. As can be seen, the hotspot temperature sharply rises, while the measurable point follows with a remarkable delay and a slower dynamic. In light of

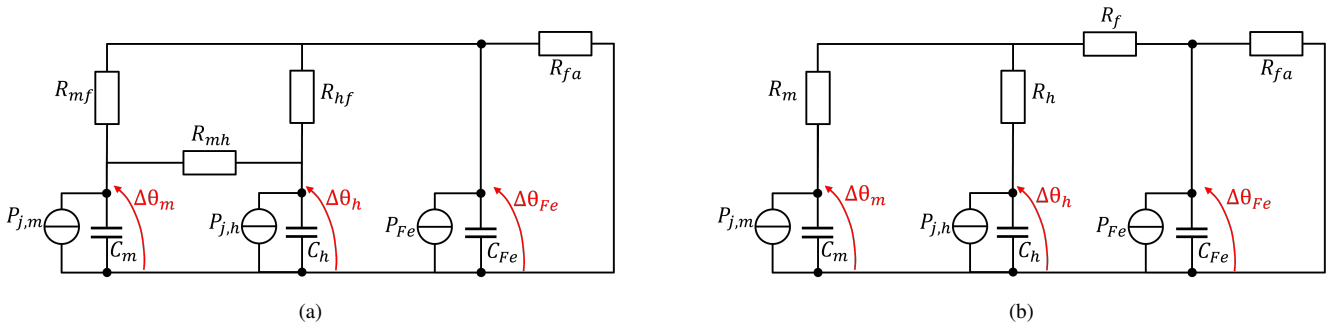

Fig. 2. Proposed LPTN for the hotspot temperature observer. (a) Physical model, delta connected. (b) Equivalent star connection, for calibration purposes.

this behavior, and since the hotspot temperature is generally unknown, a large safety margin is often required when defining the motor current and torque ratings, to avoid thermal failures.

The thermal models available in the literature can be classified into two main categories [16]. The thermal models based on Finite Element Analysis (FEA) provide an accurate and detailed representation of the temperature distribution inside the machine, but the corresponding computational burden is excessive for commercial microcontrollers. On the other hand, the system can be coarsely represented through Lumped-Parameter Thermal Networks (LPTN) [17], with a low definition of the motor parts, but requiring a largely lighter computational effort compatible with real-time execution. A common drawback of most of the LPTN present in the literature [8] is that the corresponding thermal parameters, which define the network, are often unknown and difficult to be evaluated through experimental tests.

This work proposes a novel observer based on an advanced LPTN, capable of dynamically estimating the temperature of the hottest point of the stator winding during the drive operation. This permits fully exploiting the transient overload capability of the drive, still guaranteeing high reliability and minimizing the risk of thermal failure. An analytical solution of the LPTN is provided, thus permitting a simple and fast implementation in industrial microcontrollers. Moreover, the proposed observer is directly calibrated based on experimental measurements. The proposal is verified both through FEA and experimental tests.

II. Motor Under Test and FEA Analysis

The machine under test is a high-performance PMSM for traction applications. At first, a thermal analysis of the motor was conducted using accurate thermal FEAs [18]. This permitted to identify the position of the most critical winding hotspot. The detailed motor geometry and materials, which are essential requirements for the FEA model, have been provided directly by the carmaker, but are covered by industrial property and cannot be disclosed here. For the same reason, every physical quantity is reported in the paper as normalized per unit (pu), with the rated values defined by the FEA model.

After this first analysis, a motor prototype was manufactured and thermally characterized according to [19], [20]. The thermal characterization included a Short-Time Thermal Transient (STTT) test [20] and a steady state (SS) test, both requiring DC motor supply.

In the remarkable version, only one thermistor is employed in an accessible point of the winding thermally close to the cooling system, so the measured temperature is lower than the average and hotspot temperatures. This is in accordance with the plot depicted in Figure 1. In the prototype under test, six additional thermistors permit experimentally mapping its thermal gradient, including the hotspot point identified by the FEA analysis.

A. Motor Model and FEA Simulations

The motor under test was accurately simulated both through a 3D LPTN and through dedicated thermal FEAs, using the software provided by [18]. The 3D LPTN presents a high number of nodes, permitting a precise representation of the motor and the cooling system. The 3D LPTN well describes the radial and longitudinal thermal gradients, with the thermal resistances and capacitances of the network defined by the motor geometry and materials. On the other side, the FEA analysis was carried in 2D, focusing on the motor section.

III. Proposed Hotspot Temperature Observer

The goal of this work is to design a temperature observer capable of dynamically estimating the winding hotspot temperature based on the thermistor placed in an accessible point of the winding and the estimate of the stator losses. With this respect, the thermal coupling between the stator and the rotor can be disregarded, being the stator-to-rotor thermal time constant considerably slower than the thermal coupling between the measurable and hotspot winding points. This assertion was confirmed both by FEA and experimental evidence. Therefore, the proposed observer only considers the stator thermal model.

The proposed LPTN is presented in Figure 2a. The key assumption is to split the stator winding in two sections, each of them considered at uniform temperature. The first section, labeled with the subscript m, is at the measurable temperature θ_m, while the second one, indicated with the subscript h, is at the unknown hotspot temperature θ_h. Each section has a thermal capacitance C_m, C_h and the associated Joule loss P_{jm}, P_{jh}, both proportional to the corresponding winding

volume. The aggregate of C_m and C_h constitutes the total winding thermal capacitance C_w:

$$\begin{cases} C_h &= x \cdot C_w \\ C_m &= (1-x) \cdot C_w \end{cases} \tag{1}$$

$$0 < x < 1 \tag{2}$$

being x the fraction of the winding associated with the hotspot. Similarly, for copper losses:

$$\begin{cases} P_{jh} &= x \cdot P_j \\ P_{jm} &= (1-x) \cdot P_j \end{cases} \tag{3}$$

where P_j aggregates the stator AC and DC copper losses. The stator iron thermal capacitance C_{Fe} and temperature θ_{Fe} are also introduced. The thermal resistances R_{mf} and R_{hf} model the thermal coupling between the cold and hot winding sections and the stator iron, R_{mh} the interaction between the two winding sections and R_{fa} represents the iron-to-ambient thermal resistance.

The problem is solved in terms of overtemperature with respect to the ambient temperature θ_a:

$$\begin{cases} \Delta\theta_h &= \theta_h - \theta_a \\ \Delta\theta_m &= \theta_m - \theta_a \\ \Delta\theta_{Fe} &= \theta_{Fe} - \theta_a \end{cases} \tag{4}$$

The adopted LPTN, depicted in Figure 2a, is a good representation of the physical thermal behavior of the stator winding. Anyway, for calibration and real-time implementation purposes, it is convenient to apply a $\Delta - Y$ transformation to the three resistances R_{mf}, R_{hf} and R_{mh}, leading to the LPTN reported in Figure 2b:

$$\begin{cases} R_m = \dfrac{R_{mf} \cdot R_{mh}}{R_{mf} + R_{mh} + R_{hf}} \\ R_h = \dfrac{R_{hf} \cdot R_{mh}}{R_{mf} + R_{mh} + R_{hf}} \\ R_f = \dfrac{R_{mf} \cdot R_{hf}}{R_{mf} + R_{mh} + R_{hf}} \end{cases} \tag{5}$$

It is worth mentioning that the two LPTNs in Figures 2a and 2b are analytically equivalent.

IV. Observer Design and Calibration

The proposed observer, reported in Figure 3, is a Multiple Input Single Output (MISO) system with three inputs, i.e. the measured overtemperature $\Delta\theta_m$ and the estimated Joule and iron losses P_j, P_{Fe}, and a single output, i.e. the observed hotspot overtemperature $\Delta\theta_h$. Since the thermal parameters do not considerably vary with the temperature, at least in the feasible range of operation of the drive, the system is linear and the effects superposition holds. The observer dynamic is based on the LPTN in Figure 2b, solved in the Laplace domain:

$$\hat{\theta}_h = \left.\frac{\hat{\theta}_h}{\theta_m}\right|_{\theta_m} \cdot \theta_m + \left.\frac{\hat{\theta}_h}{P_j}\right|_{P_j} \cdot P_j + \left.\frac{\hat{\theta}_h}{P_{Fe}}\right|_{P_{Fe}} \cdot P_{Fe} \tag{6}$$

$$\hat{\Delta\theta}_h = H_\theta \cdot \Delta\theta_m + H_j \cdot P_j + H_{Fe} \cdot P_{Fe} \tag{7}$$

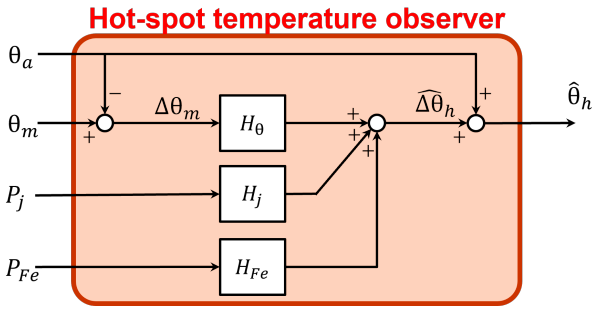

Fig. 3. Block diagram of the MISO hotspot temperature observer.

The three transfer functions can be explicated as:

$$\hat{\Delta\theta}_h = \frac{(a_\theta s + b_\theta)\,\Delta\theta_m + (a_j s + b_j)\,P_j + b_f P_{Fe}}{p_1 s^2 + p_2 s + p_3} \tag{8}$$

The two transfer functions H_θ and H_j present one zero, the numerator of H_{Fe} is real and the three transfer functions share the same two poles, i.e. the poles of the physical system. Altogether, the LPTN solution (8) presents seven parameters, which can be analytically determined based on the four thermal resistances and three capacitances:

$$\begin{cases} a_\theta = R_{fa} R_f C_{Fe} \\ b_\theta = R_{fa} + R_f \\ a_j = R_{fa}\,(R_f R_m + R_f R_h + R_m R_h)\,C_{Fe} \\ b_j = R_f R_m + R_f R_h + R_m R_h + R_m R_{fa} + R_h R_{fa} \\ b_f = R_m R_f a \\ p_1 = C_{Fe} C_h R_{fa}\,(R_h R_f + R_m R_f + R_h R_m) \\ p_2 = C_{Fe} R_{fa}\,(R_f + R_m) + \\ \quad + C_h\,(R_h R_f + R_m R_f + R_h R_m + R_h R_{fa} + R_m R_{fa}) \\ p_3 = R_f + R_m + R_{fa} \end{cases} \tag{9}$$

An experimental-based calibration procedure is proposed here for determining the LPTN parameters. The calibration procedure is based on two simple characterization tests: the STTT [19] and the SS tests, as described in the following Sections. In both cases, the motor is excited with a DC power supply, but if the STTT focuses on the initial part of the thermal transient, the SS test detects the regime measured, average and hotspot temperatures.

A. Parameters measurement

1) ***Short Time Thermal Transient test:*** The improved STTT described in [20] permits to determine the three capacitances C_m, C_h and C_{Fe} and an equivalent winding-to-iron thermal resistance, called R_{eq}. This procedure well covers the case of high-power traction motors with advanced cooling systems and high-rate heat exchange.

The three phases are connected in series, in order to ensure an homogeneous heating of the machine. If the output terminals of the three phases are not available, as common for traction motors, and the series connection of the phases is not possible, [20] proposes an alternative testing configuration, equivalent to the series excitation. The series of the three

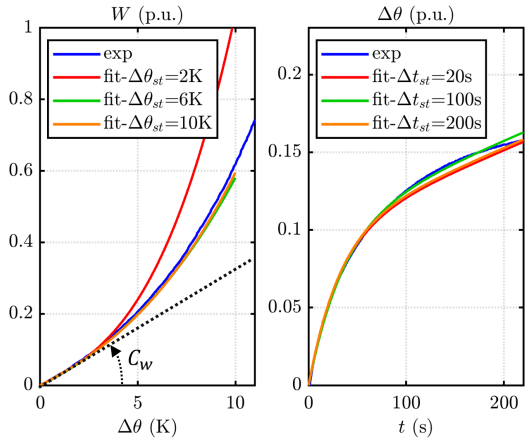

Fig. 4. Results of the STTT test [20]: $W(\Delta\theta)$ and $\Delta\theta(t)$. The measured energy and temperature rise are interpolated on varying $\Delta\theta_{st}$ and Δt_{st} respectively.

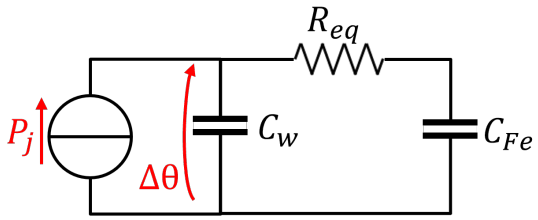

Fig. 5. Equivalent LPTN for the improved STTT test.

phases is supplied with a DC current, having an amplitude compatible with the nominal thermal current of the motor, thus producing a measurable temperature rise. During the test, the DC current i_{dc} and voltage v_{dc} are measured, computing the DC resistance R_{dc} and the corresponding Joule loss P_j. The average winding temperature is estimated from the resistance variation:

$$\theta = \frac{R_{dc}}{R_o}(234.5 + \theta_o) - 234.5 \tag{10}$$

where θ_o is the motor starting temperature, and R_o the corresponding winding resistance. The energy loss is computed by integrating P_j with respect to the time:

$$W = \int_{t_0}^{t} P_j \, dt \tag{11}$$

where t_0 corresponds to the start of DC excitation, associated with zero energy loss.

The STTT only considers the first time frame of excitation, called Δt_{st} [20], which is in the order of a few minutes. In this initial transient only, the thermal behavior of the motor is interpreted with the simplified LPTN in Figure 5. The total winding thermal capacitance C_w is computed from the initial derivative of the dissipated energy Vs overtemperature, while the iron capacitance C_{Fe} and the equivalent resistance R_{eq} are retrieved from the temperature rise evolution. All the details can be found in [20], where the same motor prototype was adopted. The plots show the measured energy and temperature rise (in blue) fitted considering different over temperature $\Delta\theta_{st}$ and time Δt_{st} intervals, as defined in [20]. Note that the computed C_w, C_{Fe} and R_{eq} are almost independent of the considered time and temperature intervals.

*2) **DC Steady State test**:* The DC Steady State test requires the same excitation and measurement setup used for the STTT, so the STTT and SS tests can be combined into a single test. If the STTT focuses on the initial thermal transient, i.e. the first few minutes of DC excitation, the SS test aims at measuring the winding temperature when the thermal regime is reached.

The thermal system is again interpreted through the LPTN in Figure 2b. Being at steady state, all the capacitances act as an open circuit and can be removed, while there are not iron losses due to the DC motor excitation. Therefore, for the SS test only the LPTN in Figure 2b can be simplified as the equivalent circuit shown in Figure 6. The series of the thermal resistances R_f and R_{fa} is called R_{ff}.

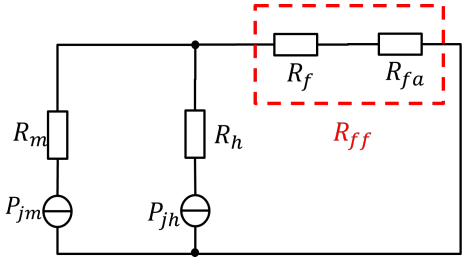

Fig. 6. Equivalent LPTN for the DC steady state test.

The steady state solution of the network, again written in terms of temperatures, is:

$$\begin{cases} \Delta\theta_m^{ss} = P_j R_{ff} + (1-x) P_j R_m \\ \Delta\theta_h^{ss} = P_j R_{ff} + x P_j R_h \end{cases} \tag{12}$$

Where $\Delta\theta_m^{ss}$ and $\Delta\theta_h^{ss}$ are the steady state over temperatures of the measurable and the hotspot points. The equivalent steady state resistances R_m^{ss} and R_h^{ss} and the parameter y are introduced as follows:

$$\begin{cases} R_m^{ss} = \dfrac{\Delta\theta_m^{ss}}{P_j} = R_{ff} + (1-x) R_m \\ R_h^{ss} = \dfrac{\Delta\theta_h^{ss}}{P_j} = R_{ff} + x R_h \end{cases} \tag{13}$$

$$y = \frac{R_f}{R_{ff}} \tag{14}$$

B. Hotspot observer calibration

To summarize, the STTT permits estimating C_w, C_{Fe} and R_{eq}, while the SS test provides R_m^{ss} and R_h^{ss}. Based on these measured quantities, and on the two coefficients x and y, the thermal parameters of the proposed hotspot temperature estimator in Figure 2b can be analytically retrieved, thus calibrating the hotspot observer through (9).

In particular, considering the results of the STTT, the capacitance C_h and C_m are determined according to (1). Still based on the STTT, i.e. on the initial part of the thermal transient, the winding temperature can be considered uniform, thus neglecting the difference between θ_m and θ_h. Therefore,

based on the LPTN in Figure 2b, the equivalent thermal resistance estimated by the STTT can be interpreted as:

$$R_{eq} = R_f + R_m \parallel R_h \tag{15}$$

Moreover, by manipulating (13), all the resistances of the LPTN can be evaluated and expressed as a function of the x and y parameters:

$$\begin{cases} R_{fa} = R_{eq} \cdot \dfrac{1-y}{y} \\ R_m = \dfrac{R_m^{ss} - \dfrac{R_{eq}}{y}}{(1-x)} \\ R_h = \dfrac{R_h^{ss} - \dfrac{R_{eq}}{y}}{x} \end{cases} \tag{16}$$

To guarantee a physical meaning of the LPTN parameters, i.e. imposing all the thermal capacitances and resistances being greater than zero, and considering $R_h^{ss} > R_m^{ss}$, the parameter y is bounded as follow:

$$\frac{R_{eq}}{R_m^{ss}} < y < 1 \tag{17}$$

Overall, the LPTN parameters are fully calibrated based on the STTT and SS tests and the two parameters x and y, which are the only two coefficients determined based on the user's experience. Nevertheless, according to (2) and (17), the parameters x and y are bounded in a narrow range, thus simplifying the tuning procedure.

Once the coefficients are determined, the hotspot temperature observer is implemented following the block diagram in Figure 3, which can be easily discretized according to (8),(9) and embedded in the motor control algorithm, for real-time hotspot temperature monitoring during the drive operation.

V. Simulation and Experimental Results

The validation of the proposal was run in parallel based on the motor FEA model and in experiments. The adopted test bench, depicted in Figure 7, is capable of finely regulating the coolant temperature of the machine.

The STTT and SS tests were executed, both in FEA simulation and in experiments, and for each case the proposed temperature observer was calibrated according to the procedure detailed in Section IV-B. It should be noted that the simulations and the experiments led to two different parameters set for the observer calibration, due to the discrepancies between the FEA model and the real machine.

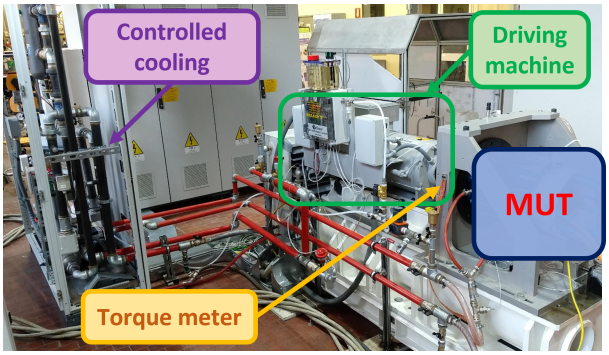

Fig. 7. Test bench adopted for experimental validation.

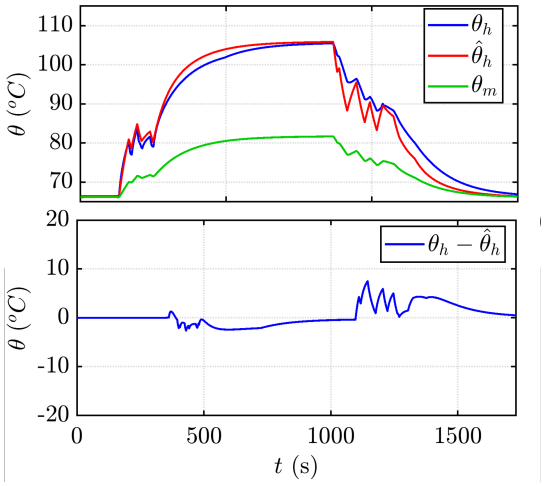

Fig. 8. Temperature prediction based on FEA simulation. Blue and red: measured and estimated hotspot temperature; green: accessible measurement point. Lower plots: temperature estimation error.

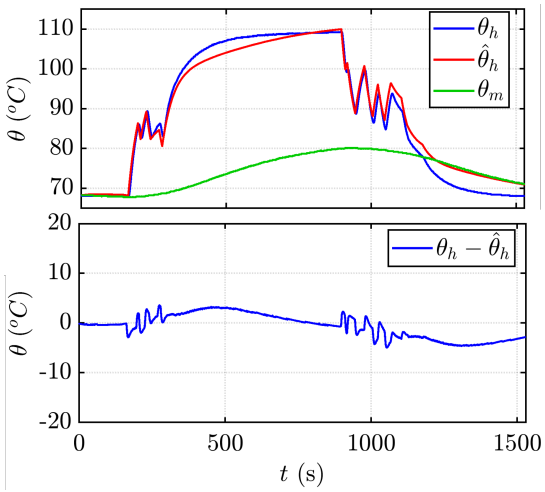

Fig. 9. Temperature prediction based on the experimental test. Blue and red: measured and estimated hotspot temperature; green: accessible measurement point. Lower plots: temperature estimation error.

Once the hotspot temperature observer was calibrated, a typical load cycle was considered, depicted in Figures 8 and 9 for the FEA and experimental test respectively, where a sequence of different idle periods and load torques are applied, corresponding to different motor losses. Due to hardware limitations, only a partial load could be applied in experiments, so the motor did not reach its maximum temperature. Anyway, the difference between the measurable and hotspot temperatures was clearly visible, both in simulation and in experiments.

The simulation and experimental results are reported in Figure 8 and 9, respectively. As said, the prototype embeds a number of thermistors, which permit monitoring the hotspot

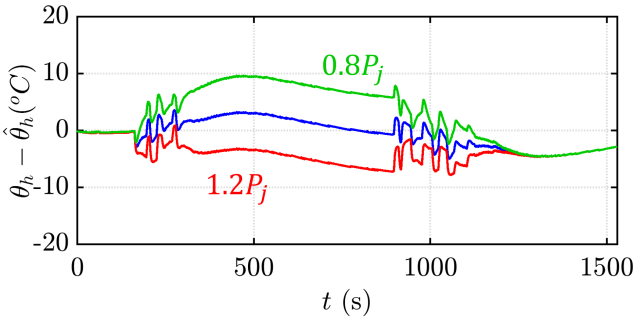

Fig. 10. Sensitivity of temperature estimation error under uncertain P_j.

temperature, while only one thermistor is available in the final application. In both simulation and experimental tests, the hotspot temperature dynamic is considerably faster than the measurable point, with a significant thermal gradient. Nevertheless, the proposed observer is capable of accurately tracking the hotspot temperature both under transient and steady state conditions, with a transient estimation error in the order of 5°C.

Finally, based on the same load cycle, a sensitivity analysis was conducted based on experimental results, assuming a $\pm 20\%$ error in the Joule loss estimation. Figure 10 reports the corresponding errors in the θ_h estimation. Despite the relevant inaccuracy of the input losses, which is over the realistic scenario in automotive, the estimation error remains within acceptable ranges.

VI. Conclusion

High power density motors frequently present relevant winding temperature hotspot, so the thermal gradient cannot be neglected. A direct measurement of the hotspot temperature is often unfeasible, as this is normally not accessible. To avoid thermal failures, a relevant safety margin is often required in the definition of the rated current and torque. This work proposes an effective observer for real-time monitoring of the hotspot winding temperature, based on an advanced LPTN and calibrated based on experimental commissioning tests, to enable a full exploitation of the machine. The LPTN consists of 7 parameters: 3 capacitances and 4 resistances and their evaluation and calibration procedure is fully described including experimental tests and post-processing computations. The hotspot observer is validated both against simulated and experimental drive cycles, showing good accuracy even under erroneous Joule loss estimation. Moreover, the observer can be directly implemented into the motor control due to its very low computational effort.

Acknowledgment

The research has been conducted with the support of Power Electronics Innovation Center (PEIC) of Politecnico di Torino.

References

[1] S. Ramarathnam, A. K. Mohammed, B. Bilgin, A. Sathyan, H. Dadkhah, and A. Emadi, "A review of structural and thermal analysis of traction motors," *IEEE Transactions on Transportation Electrification*, vol. 1, no. 3, pp. 255–265, 2015.

[2] C. Rhebergen, B. Bilgin, A. Emadi, E. Rowan, and J. Lo, "Enhancement of electric motor thermal management through axial cooling methods: A materials approach," in *2015 IEEE Energy Conversion Congress and Exposition (ECCE)*, 2015, pp. 5682–5688.

[3] A. Tikadar, D. Johnston, N. Kumar, Y. Joshi, and S. Kumar, "Comparison of electro-thermal performance of advanced cooling techniques for electric vehicle motors," *Applied Thermal Engineering*, vol. 183, p. 116182, 2021.

[4] P.-O. Gronwald and T. A. Kern, "Traction motor cooling systems: A literature review and comparative study," *IEEE Transactions on Transportation Electrification*, vol. 7, no. 4, pp. 2892–2913, 2021.

[5] R. Leuzzi, P. Cagnetta, S. Ferrari, P. Pescetto, G. Pellegrino, and F. Cupertino, "Transient overload characteristics of pm-assisted synchronous reluctance machines, including sensorless control feasibility," *IEEE Transactions on Industry Applications*, vol. 55, no. 3, pp. 2637–2648, 2019.

[6] V. Madonna, A. Walker, P. Giangrande, G. Serra, C. Gerada, and M. Galea, "Improved thermal management and analysis for stator end-windings of electrical machines," *IEEE Transactions on Industrial Electronics*, vol. 66, no. 7, pp. 5057–5069, 2019.

[7] Y. Ji, P. Giangrande, W. Zhao, V. Madonna, H. Zhang, and M. Galea, "Determination of hotspot temperature margin for rectangular wire windings considering insulation thermal degradation and partial discharge," *IEEE Transactions on Transportation Electrification*, pp. 1–1, 2023.

[8] D. Liang, Z. Q. Zhu, B. Shao, J. Feng, S. Guo, Y. Li, and A. Zhao, "Tracking of winding and magnet hotspots in spmsms based on synergized lumped-parameter and sub-domain thermal models," *IEEE Transactions on Energy Conversion*, vol. 37, no. 3, pp. 2147–2161, 2022.

[9] A. Sierra-Gonzalez, P. Pescetto, F. Alvarez-Gonzalez, B. Heriz, E. Trancho, H. Lacher, E. Ibarra, and G. Pellegrino, "Full-speed range control of a symmetrical six-phase automotive ipmsm drive with a cascaded dc-link configuration," *IEEE Transactions on Industry Applications*, vol. 59, no. 3, pp. 3413–3424, 2023.

[10] F. Stella, G. Pellegrino, and E. Armando, "Coordinated on-line junction temperature estimation and prognostic of sic power modules," in *2018 IEEE Energy Conversion Congress and Exposition (ECCE)*, 2018, pp. 1907–1913.

[11] D. Reigosa, D. Fernández, M. Martínez, J. M. Guerrero, A. B. Diez, and F. Briz, "Magnet temperature estimation in permanent magnet synchronous machines using the high frequency inductance," *IEEE Transactions on Industry Applications*, vol. 55, no. 3, pp. 2750–2757, 2019.

[12] O. Wallscheid, "Thermal monitoring of electric motors: State-of-the-art review and future challenges," *IEEE Open Journal of Industry Applications*, vol. 2, pp. 204–223, 2021.

[13] N. Z. Popov, S. N. Vukosavic, and E. Levi, "Motor temperature monitoring based on impedance estimation at pwm frequencies," *IEEE Transactions on Energy Conversion*, 2014.

[14] F. Stella, G. Pellegrino, and E. Armando, "Three-phase sic inverter with active limitation of all mosfets junction temperature," *Microelectronics Reliability*, vol. 110, p. 113659, 2020. [Online]. Available: https://www.sciencedirect.com/science/article/pii/S002627141931128X

[15] T. Dong, X. Zhang, C. Zhu, Y. Lu, and M. Li, "Improved hotspot monitoring method for thermal management system of automotive traction motor," *IET Electric Power Applications*, vol. 14, no. 11, pp. 2255–2262, 2020.

[16] C. Kral, A. Haumer, M. Haigis, H. Lang, and H. Kapeller, "Comparison of a cfd analysis and a thermal equivalent circuit model of a tefc induction machine with measurements," *IEEE Transactions on Energy Conversion*, vol. 24, no. 4, pp. 809–818, 2009.

[17] C. Sciascera, P. Giangrande, L. Papini, C. Gerada, and M. Galea, "Analytical thermal model for fast stator winding temperature prediction," *IEEE Transactions on Industrial Electronics*, vol. 64, no. 8, pp. 6116–6126, 2017.

[18] Motor Design Ltd, "Motor-CAD Software." [Online]. Available: https://www.motor-design.com

[19] P. Pescetto, S. Ferrari, G. Pellegrino, E. Carpaneto, and A. Boglietti, "Winding thermal modeling and parameters identification for multithree

phase machines based on short-time transient tests," *IEEE Transactions on Industry Applications*, vol. 56, no. 3, pp. 2472–2480, 2020.

[20] P. Pescetto, G. Dilevrano, G. Pellegrino, and A. Boglietti, "Improved short time thermal transient model and testing procedure for high power density motors," in *2023 IEEE International Electric Machines and Drives Conference (IEMDC)*, 2023.